PHYSICS OF FLUIDS **28**, 013303 (2016)

Effect of flexibility on the growth of concentration fluctuations in a suspension of sedimenting fibers: Particle simulations

Harishankar Manikantan and David Saintillan
Department of Mechanical and Aerospace Engineering, University of California San Diego, La Jolla, California 92093, USA

(Received 7 May 2015; accepted 9 December 2015; published online 7 January 2016)

Three-dimensional numerical simulations are performed to study the stability of a sedimenting suspension of weakly flexible fibers. It is well known that a suspension of rigid rods sedimenting under gravity at low Reynolds number is unstable to concentration fluctuations owing to hydrodynamic interactions. Flexible fibers, however, reorient while settling and even weak flexibility can alter their collective dynamics. In our recent work [Manikantan *et al*., "The instability of a sedimenting suspension of weakly flexible fibres," J. Fluid Mech. **756**, 935–964 (2014)], we developed a mean-field theory to predict the linear stability of such a system. Here, we verify these predictions using accurate and efficient particle simulations based on a slender-body model. We also demonstrate the mechanisms by which flexibility-induced reorientation alters suspension microstructure, and through it, its stability. Specifically, we first show that the anisotropy of the base state in the case of a suspension of flexible fibers has a destabilizing effect compared to a suspension of rigid rods. Second, a conflicting effect of flexibility is also shown to suppress particle clustering and slow down the growth of the instability. The relative magnitude of filament flexibility and rotational Brownian motion dictates which effect dominates, and our simulations qualitatively follow theoretically predicted trends. The mechanism for either effects is tied to the flexibility-induced reorientation of particles, which we illustrate using velocity and orientation statistics from our simulations. Finally, we also show that, in the case of an initially homogeneous and isotropic suspension, flexibility always acts to suppress the growth of the instability. © *2016 AIP Publishing LLC.* [http://dx.doi.org/10.1063/1.4938493]

I. INTRODUCTION

A central phenomenon in many natural and industrial processes involving complex fluids is the sedimentation of a suspension of small particles. While the settling of an isolated object in a viscous fluid is an often straightforward problem, the case of a suspension of hydrodynamically interacting particles remains an area of active research even after decades of experiments, simulations, and theoretical arguments. An extensive review of the applications, current literature, and unresolved debates can be found in the work of Guazzelli and Hinch.[1]

While the physics of a suspension of spherical particles is already non-trivial, even the simplest anisotropy in particle geometry has drastic consequences on the bulk behavior of the system. Koch and Shaqfeh[2] first showed that a suspension of rodlike particles such as spheroids or slender fibers is unstable to concentration fluctuations, a direct consequence of the fact that non-spherical particles can orient in flow and have a configuration-dependent settling velocity. This hydrodynamic instability, which has a significant impact on suspension microstructure as well as settling statistics, has since been verified in numerous experiments[3,4] and simulations,[5,6] and further extensions have also been proposed to account for the effects of container walls,[7] Brownian fluctuations,[8] and fluid inertia,[9] to list a few.

These previous studies all focused on rigid rods, which is a convenient and representative simplification of many physical systems involving the sedimentation of slender objects. Even weak fiber

compliance, however, can have a significant impact on the bulk suspension properties. A flexible filament can indeed deform in response to viscous stresses and internal elastic forces, and such deformations have complex consequences on single-particle dynamics. It was previously shown[10,11] that an isolated flexible fiber, although torque-free, spontaneously aligns perpendicular to the direction of gravity as it sediments. Apart from the obvious non-trivial trajectory that ensues, this reorientation also affects the mechanism of destabilization in a suspension of such particles as we further elucidate in this paper.

As flexibility-induced reorientation plays a central role in the simulations we perform here, we find it useful to first recapitulate the main results of our previous work[11] where this was derived. The leading dimensionless group governing the deformation of a sedimenting elastic filament is the elasto-gravitation number β, which compares the elastic bending force acting along the filament backbone to the net external gravitational force,

$$\beta = \frac{\kappa}{F_G L^2}. \tag{1}$$

Here, κ is the bending rigidity of the fiber, L its length and F_G the total gravitational force acting on it. The limit of large β corresponds to the regime of weak flexibility. In this regime, a multiple time scale asymptotic analysis was performed and revealed that the shape and translational velocity of a weakly flexible fiber is, to leading order, exactly the same as that of a rigid rod placed in the same orientation. The first correction to the rigid-rod motion comes in at $O(\beta^{-1})$ and simply acts to slowly rotate the fiber towards an orientation perpendicular to gravity. Furthermore, numerical simulations for arbitrary values of β showed that these predictions hold beyond the asymptotic regime of $\beta \gg 1$ and well into values of β smaller than unity.

This rate of reorientation due to fiber compliance, which is proportional to β^{-1}, was determined to be[11]

$$\frac{\partial \theta}{\partial t} = \frac{F_G}{8\pi\mu L^2}\frac{A}{2\beta}\sin(2\theta), \tag{2}$$

where θ is the instantaneous angle the fiber makes with the direction of gravity. Note that all orientations but those parallel or perpendicular to gravity feel this rotational velocity, causing an isolated fiber to rotate towards a terminal horizontal configuration. The fluid has viscosity μ, and $A = 3(c - 7/2)/80$ is a purely geometric constant depending on the shape of the fiber. We modeled the fiber as a slender ellipsoid of contour length L and cross-sectional radius a at its center point, which defines the slenderness parameter $c = \ln[(L/a)^2]$. The asymptotic analysis also revealed the deflection of the fiber away from a perfectly straightened state to have a maximum value of $L/256\beta$, which makes it possible to conveniently approximate the fiber contour as that of a straight rod down to values of β slightly less than 1.

We then applied our knowledge of single filament dynamics to study the stability of a suspension of weakly flexible fibers using a continuum method.[12] We followed the linear stability analysis first proposed by Koch and Shaqfeh[2] with the added ingredient of flexibility-induced reorientation. In the case of a suspension of perfectly rigid rods, the base-state distribution is uniform in space and isotropic in orientation. The effect of a spatial fluctuation in number density is to set up a vertical disturbance flow that is downward in areas of higher particle density and upward outside. This vertical shear field causes particles to rotate in such a way as to enable their orientation-dependent settling velocity to draw them into regions of already higher density, thus enhancing concentration fluctuations. Adapting this study to the case of weakly flexible fibers revealed two opposing effects of fiber flexibility. First, in the absence of fluctuations, the balance between rotational diffusion and reorientation due to flexibility gives rise to an anisotropic orientation distribution in the base state. Introducing a gravitational Péclet number $Pe = F_G L/k_B T$, and defining $\eta = APe/48(c-1)\beta$, this base-state distribution was found to be

$$\Psi_0(\theta) = m_0 \exp[-2\eta\cos^2\theta], \tag{3}$$

where m_0 is a normalization constant. We can see readily that η plays the role of an anisotropy parameter. The limit of $\eta \to 0$ renders the base state isotropic, while large values of η correspond to increasingly anisotropic distributions with a preferential alignment perpendicular to gravity — a direct

consequence of flexibility-induced reorientation. Perturbing about this configuration and following through the linear stability analysis in the continuum approach, this base-state anisotropy was shown to be the prime factor responsible for an enhanced instability as long $\beta \gtrsim 1$. The mechanism suggested was straightforward: a nearly horizontal alignment of fibers made it more likely for each to be reoriented by the disturbance fields of the others in a way as to be drawn towards regions of already higher number density. The second and opposite effect of flexibility becomes stronger as the fibers become less rigid, specifically as $\beta \lesssim 1$, when the effect of the reorientation of individual particles due to flexibility becomes comparable to that due to the disturbance field. Strong horizontal alignment then tends to hinder horizontal drift and therefore the very mechanism of growth of fluctuations. On approaching the problem asymptotically, we indeed showed that the growth rate has a $O(\beta^{-1})$ negative correction due to this "independent" effect of flexibility, contrasting it with the effect of the base state that hinges on the relative magnitude of flexibility and rotational diffusion through the parameter η.

These prior theoretical results were derived from a continuum approach where the fibers were abstracted as point forces with a director that determined their translational and rotational velocities. While this simplified model was analytically tractable and extremely insightful into the short-time growth of fluctuations, we draw in the present paper a more detailed picture using discrete particle simulations. Not only do we show the validity of the continuum theory but we also go on to elucidate the microstructural changes that the particle simulation affords us, which will in turn reveal the mechanisms involved in the enhancement or suppression of the instability. Here, again, we exploit the approximations that weak flexibility grants us — namely, that each fiber can be approximated to leading-order as a rigid rod, with the effect of flexibility entering solely through the rotational velocity in Eq. (2). This allows us to use efficient and fast methods that have been previously developed for simulating suspensions of rigid rods.[5,13]

Note that the "weak" flexibility mentioned above is measured with respect to gravitational forces. The disturbance field induced by the settling of other particles could, in principle, also deform the fibers, though we argue here that such deflections are negligible in dilute suspensions. The potential for fiber deflection due to the disturbance flow field can be assessed by comparing the viscous forces due to the flow against the elastic rigidity of the filaments. To this end, we need to determine an appropriate velocity scale. We first note that bending due the flow can at most result from quadratic variations of disturbance velocity field $\mathbf{u}_d$ in a Taylor expansion about the fiber center, the leading order contributing only to fiber translation and the linear term to rotation. The Fourier component of u_d can be estimated following Hasimoto[12,14] as $\tilde{u}_d \sim nF_G/\mu k^2$, where k is the wavelength of the perturbation and n is the fiber number density. We know from the continuum theory that waves of the size of the box (L_x) are the most unstable and therefore set $k = 2\pi/L_x$. The quadratic term in the expansion of u_d, which represents variations across the fiber length L potentially leading to deflections, is then given by

$$u_d \sim \frac{x^2}{2}\frac{d^2}{dx^2}\left(\frac{nF_G L_x^2}{\mu(2\pi)^2}\,\mathrm{e}^{i2\pi x/L_x}\right)\bigg|_{x=L}, \tag{4}$$

providing a velocity scale of $u_d \sim nF_G L^2/2\mu$. We can then compare the relative strengths of this fluid flow with the elastic rigidity of the fibers by constructing an appropriate dimensionless number. Such a number is given by the "effective viscosity"[15] defined as $\bar{\mu} = 8\pi\mu u_d L^3/\kappa$. Using the velocity scale from Eq. (4), the effective viscosity simplifies to $\bar{\mu} \sim nL^3/\beta$. Now, we know from previous works[15,16] on the deformation of flexible filaments by viscous forces that significant filament deformation occurs in the range $\bar{\mu} \gtrsim 1000$. For the range of β and nL^3 that we shall restrict ourselves to in the current work, $\bar{\mu}$ is significantly smaller than this value, and filament deformations by the disturbance flow can thus be safely neglected.

The paper is organized as follows. In Sec. II, we describe the slender-body model used to describe the dynamics of each fiber and its hydrodynamic interaction with every other fiber in the suspension. The numerical method used to integrate the configuration of the fibers in time in the presence of Brownian motion is also described there. Results from simulations are presented in Sec. III where we systematically analyze the changes in number density fluctuations and migration of particles, which reveals the mechanism of the instability. We also make use of our simulation method to consider the

evolution of a well-stirred isotropic suspension of weakly flexible particles, which was outside the purview of the linear continuum theory. Concluding remarks are given in Sec. IV.

II. SLENDER-BODY MODEL AND NUMERICAL METHOD

As previously discussed, the deflection of a fiber from a nearly straightened state is small when it is weakly flexible ($\beta \gg 1$), and we exploit this fact to model each fiber as a rigid rod with the effect of flexibility entering only through flexibility-induced reorientation. We consider a periodic collection of N fibers, where each fiber indexed by α is described entirely by the position of its center $\mathbf{x}_\alpha$ and a director $\mathbf{p}_\alpha$, which is the tangent to the filament at its center. We shall assume zero Reynolds number flow, without any particle inertia. In a dilute suspension of such particles, the leading-order effect of each particle on every other is that due to a net force on the fluid (Stokeslet) equal to its weight corrected for buoyancy and acting at the particle center. Within these approximations, it is implicit that we do not take into account the effect of the disturbance field of one fiber on the shape of another — the suspension will be assumed to be sufficiently dilute to render such effects negligible.

We use slender-body theory for Stokes flow to model the dynamics of each fiber. To non-dimensionalize the equations, we choose as characteristic scales the length of each filament L, the sedimentation time scale $8\pi\mu L^2/F_G$, and the gravitational force on a fiber F_G. We shall be primarily concerned with cases where Brownian motion is weak, hence the choice of fiber weight as the characteristic scale for force. Parametrized along its length by $s_\alpha \in [-1/2, 1/2]$, each fiber then follows the local slender-body equation[17]

$$\dot{\mathbf{x}}_\alpha + s\dot{\mathbf{p}}_\alpha - s\dot{\mathbf{p}}^s_\alpha(\mathbf{p}_\alpha) - \mathbf{u}^\infty_\alpha(\mathbf{x}_\alpha + s_\alpha\mathbf{p}_\alpha) = (\lambda_1\mathbf{I} + \lambda_2\mathbf{p}_\alpha\mathbf{p}_\alpha)\cdot\mathbf{f}_\alpha(\mathbf{x}_\alpha + s_\alpha\mathbf{p}_\alpha). \tag{5}$$

Here, $\dot{\mathbf{p}}^s_\alpha$ is the flexibility-induced reorientation velocity that depends on the instantaneous orientation of fiber α as described by Eq. (2). This can be interpreted as an external rotational velocity imposed on each rod that captures the leading order effect of elastohydrodynamic interactions. The external velocity $\mathbf{u}^\infty_\alpha$ felt by fiber α accounts for hydrodynamic interactions and is the disturbance field generated by the forces exerted on the fluid by all other fibers in the suspension as well as their periodic images. Finally, $\mathbf{f}_\alpha$ is the force distribution along the length of the fiber, and $\lambda_1 = c + 1$ and $\lambda_2 = c - 3$ are the anisotropic mobility coefficients for a slender rod. Written this way, Eq. (5) is accurate to $O(\beta^{-2})$.

The force distribution $\mathbf{f}_\alpha(s_\alpha)$ on each fiber has contributions coming from both gravity and Brownian fluctuations in the solvent. Following previous works,[5,13,18] this distribution is approximated by a truncated Legendre polynomial expansion,

$$\mathbf{f}_\alpha(\mathbf{x}_\alpha + s_\alpha\mathbf{p}_\alpha) = \mathbf{F}^{(0)}_\alpha + 12s_\alpha\mathbf{F}^{(1)}_\alpha + O(s^2_\alpha), \tag{6}$$

where $\mathbf{F}^{(n)}_\alpha$ is the nth moment of the force distribution over the length of the fiber and where only the first two moments are retained. The zeroth moment has contributions from both gravity and Brownian forces: $\mathbf{F}^{(0)}_\alpha = -\hat{\mathbf{z}} + \mathbf{F}^{(0)}_{\alpha,B}$. For the purpose of the simulation algorithm that we describe below, it is convenient to write the first moment as a sum of parts along and orthogonal to the director,

$$\mathbf{F}^{(1)}_\alpha = \mathsf{S}_\alpha\mathbf{p}_\alpha + (\mathbf{I} - \mathbf{p}_\alpha\mathbf{p}_\alpha)\cdot\mathbf{F}^{(1)}_\alpha. \tag{7}$$

This, respectively, captures the effects of a scalar stresslet $\mathsf{S}_\alpha = \mathbf{p}_\alpha\cdot\mathbf{F}^{(1)}_\alpha$ acting to "stretch" the fiber along its director, and of a torque that reorients the fiber. It is worth noting here that a net torque can only result from Brownian fluctuations; neither gravity nor its interaction with flexibility contributes to a torque over the entire body. Inverting single-fiber equation (5) above enables us to express the scalar stresslet as

$$\mathsf{S}_\alpha = -\frac{1}{\lambda_1 + \lambda_2}\int_{-1/2}^{1/2} s_\alpha\mathbf{p}_\alpha\cdot\mathbf{u}^\infty_\alpha\, ds_\alpha. \tag{8}$$

The motion of each fiber and its periodic images affects every other fiber due to long-ranged hydrodynamic interactions. This enters the dynamics of fiber α via the disturbance field $\mathbf{u}^\infty_\alpha$, which is given by

$$\mathbf{u}^{\infty}_{\alpha}(\mathbf{x}_\alpha + s_\alpha \mathbf{p}_\alpha) = \sum_{\gamma=1}^{N} \int_{-1/2}^{1/2} \mathbf{K}(\mathbf{x}_\alpha + s_\alpha \mathbf{p}_\alpha, \mathbf{x}_\gamma + s_\gamma \mathbf{p}_\gamma) \cdot \mathbf{f}_\gamma(\mathbf{x}_\gamma + s_\gamma \mathbf{p}_\gamma)\, ds_\gamma. \tag{9}$$

Here, $\mathbf{K}_{\alpha\gamma} \equiv \mathbf{K}(\mathbf{x}_\alpha + s_\alpha \mathbf{p}_\alpha, \mathbf{x}_\gamma + s_\gamma \mathbf{p}_\gamma)$ is the periodic Green's function for Stokes flow, with the direct Stokeslet contribution removed when $\alpha = \gamma$.

We now have all the ingredients needed to derive evolution equations for the position and orientation of each fiber. Calculating the zeroth and first moments of Eq. (5) yields after manipulations

$$\dot{\mathbf{x}}_\alpha = \dot{\mathbf{x}}^{s}_{\alpha} + \sum_{\gamma=1}^{N} \left[\mathbf{Q}^{(0)}_{\alpha\gamma} \cdot \mathbf{F}^{(0)}_{\gamma} + 12 \mathbf{Q}^{(1)}_{\alpha\gamma} \cdot (\mathbf{I} - \mathbf{p}_\gamma \mathbf{p}_\gamma) \cdot \mathbf{F}^{(1)}_{\gamma} + 12 \mathbf{q}_{\alpha\gamma} \mathsf{S}_\gamma \right], \tag{10}$$

$$\dot{\mathbf{p}}_\alpha = \dot{\mathbf{p}}^{s}_{\alpha} + 12 (\mathbf{I} - \mathbf{p}_\alpha \mathbf{p}_\alpha) \cdot \sum_{\gamma=1}^{N} \left[\mathbf{R}^{(0)}_{\alpha\gamma} \cdot \mathbf{F}^{(0)}_{\gamma} + 12 \mathbf{R}^{(1)}_{\alpha\gamma} \cdot (\mathbf{I} - \mathbf{p}_\gamma \mathbf{p}_\gamma) \cdot \mathbf{F}^{(1)}_{\gamma} + 12 \mathbf{r}_{\alpha\gamma} \mathsf{S}_\gamma \right]. \tag{11}$$

Here, $\dot{\mathbf{x}}^{s}_{\alpha}$ and $\dot{\mathbf{p}}^{s}_{\alpha}$ denote the linear and angular velocities of an isolated fiber under the effect of gravity and of Brownian fluctuations:

$$\dot{\mathbf{u}}^{s}_{\alpha} = (\lambda_1 \mathbf{I} + \lambda_2 \mathbf{p}_\alpha \mathbf{p}_\alpha) \cdot \mathbf{F}^{(0)}_{\alpha}, \tag{12}$$

$$\dot{\mathbf{p}}^{s}_{\alpha} = 12 \lambda_1 (\mathbf{I} - \mathbf{p}_\alpha \mathbf{p}_\alpha) \cdot \mathbf{F}^{(1)}_{\alpha} + \frac{A}{2\beta} \sin(2\theta_\alpha) \hat{\boldsymbol{\theta}}_\alpha. \tag{13}$$

Hydrodynamic interactions between fibers are captured by the sums on the right-hand sides of Eqs. (10) and (11), where $\mathbf{Q}^{(n)}_{\alpha\gamma}$, $\mathbf{R}^{(n)}_{\alpha\gamma}$, $\mathbf{q}_{\alpha\gamma}$, and $\mathbf{r}_{\alpha\gamma}$ are double integrals over pairs of fibers as described below, the former two being second-order tensors and the latter two vectors:

$$\mathbf{Q}^{(n)}_{\alpha\gamma} = \iint s^{n}_{\gamma}\, \mathbf{K}_{\alpha\gamma}\, ds_\alpha ds_\gamma, \tag{14a}$$

$$\mathbf{R}^{(n)}_{\alpha\gamma} = \iint s_\alpha\, s^{n}_{\gamma}\, \mathbf{K}_{\alpha\gamma}\, ds_\alpha ds_\gamma, \tag{14b}$$

$$\mathbf{q}_{\alpha\gamma} = \iint s_\gamma\, \mathbf{K}_{\alpha\gamma} \cdot \mathbf{p}_\gamma\, ds_\alpha ds_\gamma, \tag{14c}$$

$$\mathbf{r}_{\alpha\gamma} = \iint s_\alpha s_\gamma\, \mathbf{K}_{\alpha\gamma} \cdot \mathbf{p}_\gamma\, ds_\alpha ds_\gamma. \tag{14d}$$

Finally, we note that the stresslets on each fiber remain unknown. They are coupled through Eq. (8), which, when written out, yields the linear system,

$$(\lambda_1 + \lambda_2) \mathsf{S}_\alpha + 12\, \mathbf{p}_\alpha \cdot \sum_{\gamma=1}^{N} \left[\mathbf{r}_{\alpha\gamma}\, \mathsf{S}_\gamma \right] = -\mathbf{p}_\alpha \cdot \sum_{\gamma=1}^{N} \left[\mathbf{R}^{(0)}_{\alpha\gamma} \cdot \mathbf{F}^{(0)}_{\gamma} + 12 \mathbf{R}^{(1)}_{\alpha\gamma} \cdot (\mathbf{I} - \mathbf{p}_\gamma \mathbf{p}_\gamma) \cdot \mathbf{F}^{(1)}_{\gamma} \right]. \tag{15}$$

Advancing the configuration of the particles in the suspension involves integrating Eqs. (10) and (11) in time. To this end, we need to evaluate the integral operators in Eq. (14) as well as determine the yet unknown stresslets acting on each fiber. Solving Eq. (15) for the stresslets, in turn, also requires knowledge of the integral operators. Each of the integrals in Eq. (14) involves a three-dimensional summation of periodic Stokeslets that decay as $\sim 1/r$, which in general diverges if performed directly. Furthermore, these integrals are pairwise operators over a system of N fibers and, if calculated naively, require $O(N^2)$ operations, which can be computationally prohibitive in large systems. Here, we choose to use the Smooth Particle-Mesh Ewald (SPME) algorithm[5] to perform these operations. The algorithm relies on an Ewald summation technique to resolve the divergence of the periodic sum by decomposing it into convergent real and Fourier parts, and then applies fast Fourier transforms to accelerate the evaluation of the Fourier part. The reader is directed to the work of Saintillan *et al.*[5] for more details, and we shall only mention here that SPME reduces the cost of each such operation to approximately $O(N \log N)$.

The stresslet equation (15), which is an $N \times N$ linear system as mentioned above, forbids the use of conventional inversion techniques such as LU decomposition when SPME is used to evaluate the integrals. Indeed, the SPME algorithm forgoes the direct calculation of the entries of the matrix, but rather provides an efficient and accurate "black box" to perform matrix-vector products. This hints at

using an iterative method for the system inversion, and a convenient choice is the Generalized Minimal Residual (GMRES) method.[19] At each iteration, GMRES delegates the matrix-vector product to an external routine, which in our case can be set to the SPME algorithm, and in this way the stresslets can be determined efficiently with the same order of computational cost as SPME.

The last ingredient that is needed to complete the formulation is a description of Brownian forces. The persistence length $\ell_p = \kappa/k_BT$ of the fibers, which measures their elastic rigidity to thermal fluctuations, can be expressed in dimensionless form as

$$\frac{\ell_p}{L} = \frac{\kappa}{k_BTL} = \frac{\kappa}{F_GL^2} \times \frac{F_gL}{k_BT} = \beta \times Pe. \tag{16}$$

This demonstrates that filament distortions due to thermal fluctuations can be safely ignored as long as the product of the elasto-gravitation number and Péclet number is sufficiently large, which is the regime considered in this work. Therefore, consistent with the formulation above, we only need to account for the first two moments of the Brownian force distribution on each fiber, which affect its translational and rotational motion but not its shape. These depend on the instantaneous configuration of the suspension through the fluctuation-dissipation theorem, and thus require knowledge of the grand mobility tensor. To describe the Brownian forces, we make use of a shorthand notation and formally rewrite the evolution equations (10) and (11) as:

$$\begin{pmatrix} \dot{\mathcal{U}} \\ \dot{\mathcal{P}} \end{pmatrix} = \mathcal{M} \cdot \begin{pmatrix} \mathcal{F}^{(0)} \\ \mathcal{F}^{(1)} \end{pmatrix}, \tag{17}$$

where the left-hand side consists of a concatenation of the generalized $3N$ translational and rotational velocities $\dot{\mathcal{U}}$ and $\dot{\mathcal{P}}$. $\mathcal{M}$ is the $6N \times 6N$ grand mobility tensor corresponding to this problem, which incorporates all the dynamics, local and non-local, occurring as a result of the forces acting on the fibers; $\mathcal{F}^{(n)}$ is a $3N$ vector that is the concatenation of the nth moment of forces on each of the fibers. Note that the contribution from the stresslets S_α is implicit in $\mathcal{M}$. This notation is especially convenient in specifying the moments of the Brownian forces $\mathcal{F}_B$ following the fluctuation-dissipation theorem,

$$\left\langle \begin{pmatrix} \mathcal{F}_B^{(0)} \\ \mathcal{F}_B^{(1)} \end{pmatrix}(t) \right\rangle = \mathbf{0}, \tag{18}$$

$$\left\langle \begin{pmatrix} \mathcal{F}_B^{(0)} \\ \mathcal{F}_B^{(1)} \end{pmatrix}(t) \otimes \left(\mathcal{F}_B^{(0)} \mathcal{F}_B^{(1)} \right)(t') \right\rangle = 2\delta(t-t')\mathcal{M}^{-1}. \tag{19}$$

For the purpose of numerical evaluation, we model the generalized Brownian force vector acting during one time step Δt as

$$\begin{pmatrix} \mathcal{F}_B^{(0)} \\ \mathcal{F}_B^{(1)} \end{pmatrix} \approx \sqrt{\frac{2}{\Delta t}}\, \mathcal{B} \cdot \mathbf{w}, \tag{20}$$

where $\mathbf{w}$ is a $6N$ vector containing a Gaussian variate distribution with zero mean and unit variance, and $\mathcal{B}$ is an approximation to the square root of the inverse of the grand mobility tensor, $\mathcal{B} \cdot \mathcal{B}^T = \mathcal{M}^{-1}$.

Finding $\mathcal{B}$ is not a straightforward exercise, again because the coefficients of the grand mobility matrix are not known explicitly. In previous works,[8,20–22] this problem was overcome by using a spectral approximation to the matrix square root, and by expressing $\mathcal{B}$ in terms of a polynomial expansion involving the grand mobility matrix, the action of which on any vector can then be performed using SPME. In the same spirit, we resort here to a simpler approximation that exploits the diluteness of the suspension: specifically, we decompose the grand mobility matrix into a dominant contribution from the independent and local viscous drag on each fiber and a weaker contribution due to far-field hydrodynamic interactions. To illustrate this approximation, it is convenient to abstract the $6N \times 6N$ matrix $\mathcal{M}$ as a $N \times N$ matrix $\mathbf{M}$, each element M_{ij} of which is a 6×6 sub-matrix describing the hydrodynamic coupling between fibers i and j. Formally, we can then decompose the matrix into a sum of local and non-local parts,

$$\mathbf{M} = \mathbf{L} + \epsilon\mathbf{H}, \tag{21}$$

where $\epsilon \ll 1$ because, in a dilute suspension, the contribution from hydrodynamic interactions is small compared to the local effect due to viscous drag. Here, $\mathbf{L}$ has only diagonal entries, each of which represents the known 6×6 local mobility tensor of individual fibers, while $\mathbf{H}$ contains the off-diagonal components accounting for interactions. To proceed, we seek an approximation to the inverse of $\mathbf{M}$ of the form $\mathbf{M}^{-1} = \mathbf{A} + \epsilon\mathbf{K}$. Using the fact that $\mathbf{M} \cdot \mathbf{M}^{-1} = \mathbf{I}$ and retaining only terms up to order ϵ, it is straightforward to see that $\mathbf{A} = \mathbf{L}^{-1}$ and $\mathbf{K} = -\mathbf{L}^{-1} \cdot \mathbf{H} \cdot \mathbf{L}^{-1}$. Finding the square root is then a similar exercise, where we seek a matrix $\mathbf{B} = \mathbf{N} + \epsilon\mathbf{J}$ which satisfies $\mathbf{B} \cdot \mathbf{B}^T = \mathbf{M}^{-1}$. We easily find that $\mathbf{N} = \mathbf{L}^{-1/2}$ and $\mathbf{J} = -1/2\, \mathbf{L}^{-1/2} \cdot \mathbf{H} \cdot \mathbf{L}^{-1}$.

Now, recall that each diagonal entry of $\mathbf{L}$ is not a scalar but a local 6×6 mobility matrix corresponding to a given fiber. This matrix is known explicitly using Eqs. (12) and (13) and can be inverted analytically. The final form of the inverse square root as used in the matrix-vector operation in Eq. (20) above is then

$$\mathbf{B} \cdot \mathbf{w} \approx \mathbf{L}^{-1/2} \cdot \mathbf{w} - \frac{1}{2}\, \mathbf{L}^{-1/2} \cdot \mathbf{H} \cdot (\mathbf{L}^{-1} \cdot \mathbf{w}), \tag{22}$$

where we have omitted the ϵ in the second term. Using Eq. (22), the evaluation of the generalized force vector $\mathcal{F}_B$ now only requires local operations (of powers of the matrix $\mathbf{L}$) as well as a small number of calls to the SPME routine (to evaluate the action of the matrix $\mathbf{H}$). Finally, we use the second-order midpoint algorithm of Fixman[23] and Grassia *et al.*[24] for time integration of Eqs. (10) and (11), which accurately treats the drift term[8,22] known to arise in Brownian dynamics simulations of systems with configuration-dependent mobilities.

III. RESULTS AND DISCUSSION

Our main motivation for this study is the verification of the predictions of the continuum model of Manikantan *et al.*,[12] and so we reiterate here the main results of the linear stability analysis following that model. Flexibility-induced reorientation has two conflicting effects on suspension stability. First, the base-state distribution in a suspension of flexible fibers is anisotropic with a preferential alignment perpendicular to gravity following Eq. (3). This base state renders the suspension more unstable to number density fluctuations as compared to an isotropic suspension. The central mechanism behind the growth of fluctuations requires particles to be reoriented by the disturbance flow in a way that causes them to be drawn into regions of higher concentration. This mechanism, however, can also be hindered by the second effect wherein flexibility-induced reorientation, if sufficiently strong, acts to keep particles aligned perpendicular to gravity. As previously mentioned, this effect enters at $O(\beta^{-1})$. The relative magnitude of this reorientation with respect to rotational diffusion as well as hydrodynamic disturbances decides which effect dominates.

In order to verify the predictions of the theory using particle simulations, we set as the initial condition a homogeneous distribution in space, with an orientation distribution $\Psi(\theta)$ that depends on the values of the Péclet and elasto-gravitation numbers according to Eq. (3). In this way, we have a discrete analogue of the continuum problem and can perform direct comparisons. However, we shall also look for completeness at the evolution of a well-stirred suspension, which is expected to have an isotropic orientation distribution regardless of Pe and β — this initial condition, which is perhaps the most relevant to experiments and is addressed in Sec. III C, is not a steady base state in the continuum model and is therefore not easily addressed by a stability analysis. For the sake of illustration, we select four representative cases to parametrically study the effects of flexibility and thermal fluctuations. These cases are summarized in Table I, and we shall refer to them as cases A–D from here on. They were chosen to compare and contrast the destabilizing effect of the base state, the suppression due to flexibility-induced reorientation, and the randomizing effect of Brownian motion. Of course, the linear stability results only describe the evolution of the suspension at short times and for small perturbations away from the base state; we shall accordingly only compare the short-time statistics to the mean-field predictions.

TABLE I. The four representative cases used in the simulations to compare and contrast the different regimes of instability.

	β	Pe	Description
Case A	10^6	10^6	Benchmark case: negligible effects of flexibility or Brownian motion
Case B	10	10^6	Anisotropic base state with weak flexibility-induced reorientation
Case C	0.01	10^6	Anisotropic base state with strong flexibility-induced reorientation
Case D	10^6	100	Strong thermal fluctuations

All the simulations discussed here were performed in a periodic box of dimensions $L_x \times L_y \times L_z = 20 \times 5 \times 10$, with gravity pointing downwards in the third dimension. Unless otherwise specified, the data below are ensemble averaged over 16 simulations each of 200 fibers in a periodic box, corresponding to an effective volume fraction of $nL^3 = 0.2$. Snapshots from a set of simulations are shown in Fig. 1, where the growth of density fluctuations in the different cases described above can be assessed.

A. Number density fluctuations

The growth of number density fluctuations is a very clear feature of unstable particle suspensions. It has been observed in previous experiments as well as simulations that rigid rods tend to cluster into vertical "streamers" that sediment much faster than the average settling speed and are surrounded by clarified regions with a preferential alignment in the direction of gravity. Recall that

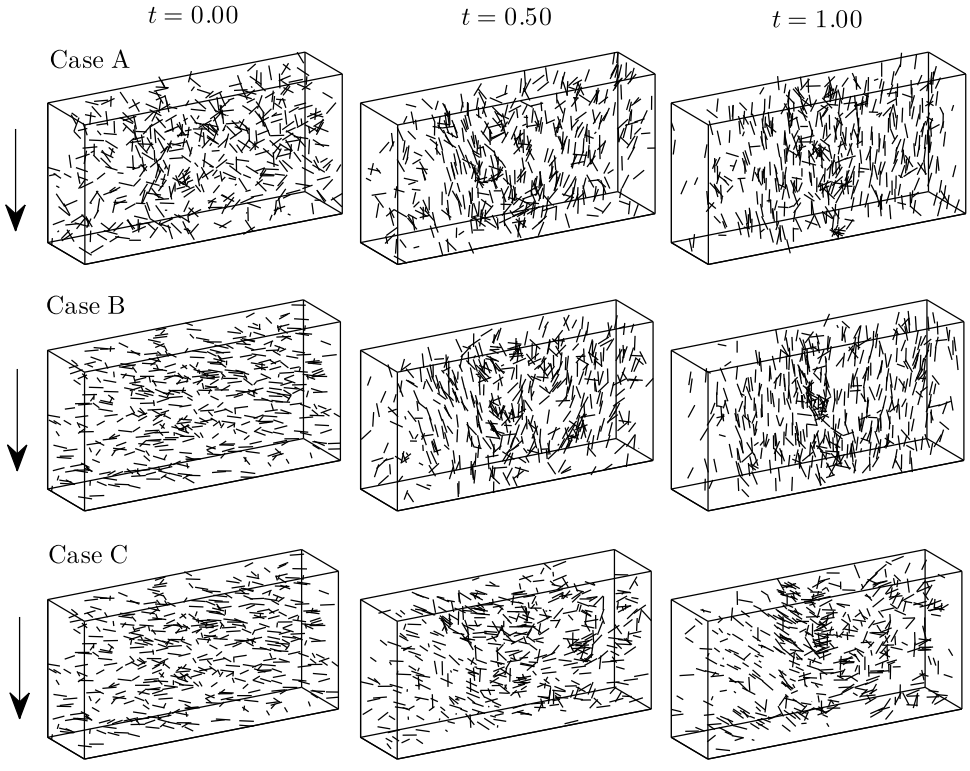

FIG. 1. Snapshots from simulations of 500 fibers in a 3-D periodic box of size $20\times5\times10$ particles lengths. Gravity acts in the direction indicated by the arrows. A larger number density of $nL^3 = 0.5$ is used here to better visualize the formation of particle clusters. Case A is the benchmark case of an isotropic suspension of rigid rods. Cases B and C depict the effect of flexibility, the former being when the anisotropic base state dominates and enhances the instability, while the latter is when the rate of reorientation dominates and impedes particle clustering. The initial spatial distribution is homogeneous and identical at $t = 0$; the orientations, however, follow the appropriate distribution of Eq. (3).

case A corresponds exactly to this well-studied situation, and many of these features are indeed visible in Fig. 1.

In order to systematically quantify the spatial non-uniformity of the particles in the system, we define a measure $d(t)$ as the standard deviation of the number density distribution across cubic inspection boxes of a given size and placed at arbitrary locations throughout the simulation domain. This quantity is normalized by the standard deviation of the corresponding Poisson distribution, so that $d = 1$ for a randomly distributed suspension of particles. The size of the inspection box was checked to have no qualitative impact on the results shown here, all of which used cubical test sections of volume $(2.5L)^3$, where L is the length of a fiber. Physically, d is a qualitative index of the perturbations to the number density, playing the analogue of the magnitude of concentration fluctuations in the mean-field model.

Figure 2(a) shows this quantity for the four representative cases over the length of the entire simulation. Clearly, all cases are destabilized although at different rates. Over a short time scale, these differences are significant. Over long times, however, and especially after persistent clusters are formed, d is no longer found to characterize the minor differences between the four cases. We are primarily interested in the effects of flexibility on the initial growth of fluctuations, and so we look at the short-time behavior of cases A–C in Fig. 2(b). Recall that $d(t)$ is a proxy for the magnitude of concentration fluctuations, and we use it to extract a linear "growth rate" by approximating it as $d(t)/d(0) = \exp \varsigma t \approx 1 + \varsigma t$ for short times. We see that the predictions of the continuum theory are qualitatively reproduced in these simulations. As compared to the case of a suspension of initially isotropically oriented rods (case A), an anisotropic suspension with weak flexibility-induced reorientation (case B) is found to be more unstable to concentration fluctuations due to the effect of the base state. For yet smaller values of β (more flexible filaments), this base-state effect is overtaken by the independent effect of flexibility in case C, where reorientation under gravity is strong enough to hinder the instability.

A more quantitative comparison to the theory can be obtained by investigating the variations of the measured growth rate in the Pe–β parameter space. A theoretical phase diagram was presented by Manikantan *et al.*[12] and is overlaid in Fig. 3 with data from simulations, where the radii of the circles are proportional to ensemble averages of ς across 16 distinct simulations at the corresponding values of β and Pe. In other words, since ς is a qualitative analogue to the linear growth rate in the continuum model, a larger circle in Fig. 3 corresponds to a suspension that on average is destabilized faster. The trends are obvious and excellently corroborate the theoretical predictions. Moving down along the vertical Pe axis demonstrates that the suspension is always stabilized by thermal randomization. On the other hand, the dependence upon β is non-monotonic. As β is decreased from large values (limit

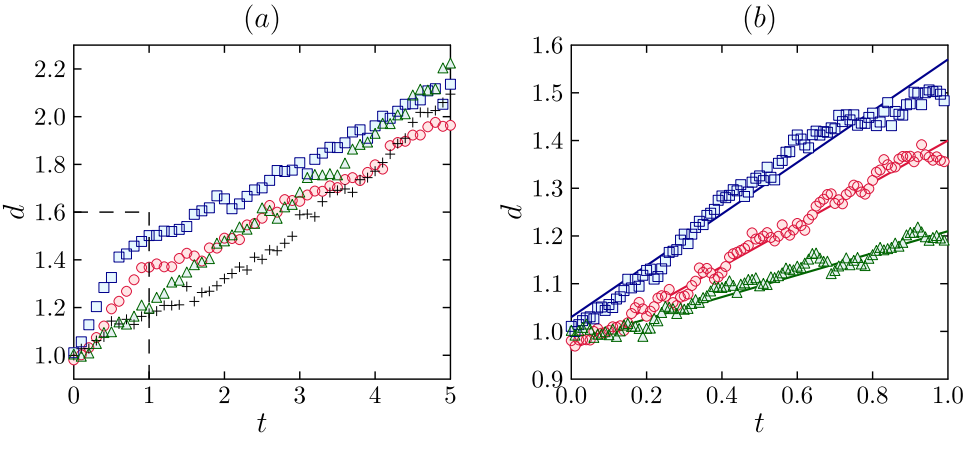

FIG. 2. (a) Growth of number density fluctuations as visualized by the measure $d(t)$. Here, case A is in red (○), B in blue (□), C in green (△), and D in black (+). $d = 1$ corresponds to a homogeneous spatial distribution of fibers at $t = 0$, and this is seen to be immediately disturbed in all cases. (b) A close-up of the region indicated by the dashed box in (a) shows the short-time effect of flexibility on suspension stability (cases A–C). The linear fits used to determine the growth rate ς are also shown in solid lines.

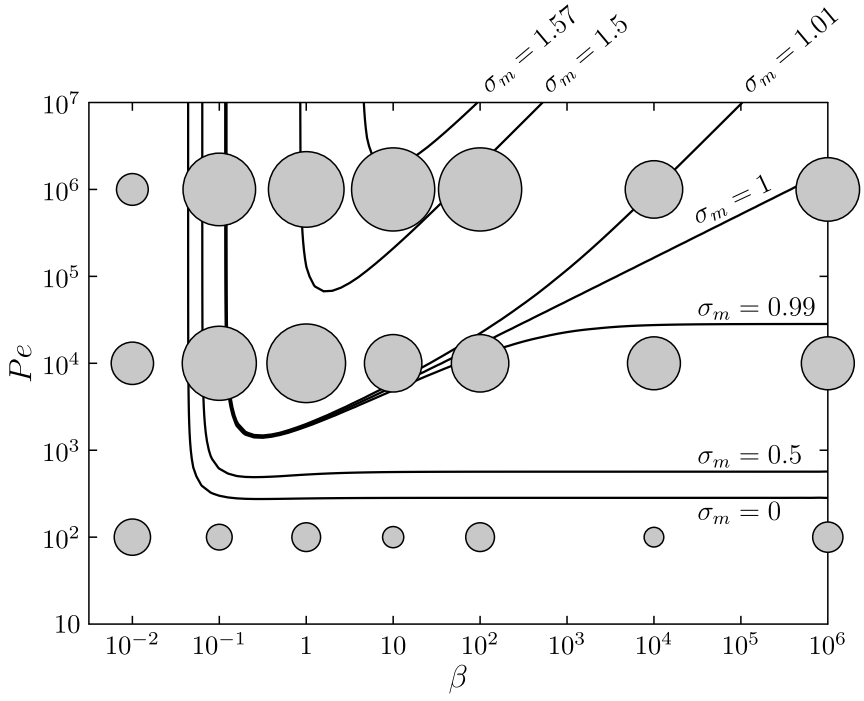

FIG. 3. A phase diagram of suspension stability in the β–Pe parameter space. The circles are proportional to the ς parameter which is a qualitative index of the growth rate of number density fluctuations in particle simulations. The contours in solid lines correspond to the linear theory of Manikantan *et al.*,[12] with predicted maximum growth rates σ_m indicated. According to the normalization used, $\sigma_m = 1$ is the theoretical growth rate when $\beta \to \infty$ and $Pe \to \infty$ (rigid non-Brownian rods).

of rigid rods), an increase in the growth rate is first seen due to an increased value of the parameter η which determines the anisotropy of the base state, until $\beta \lesssim 1$ below which the independent effect of flexibility-induced reorientation kicks in and tends to suppress the instability by resisting rotation of the fibers by the disturbance flow.

B. Horizontal particle migration

The mechanism of destabilization first described by Koch and Shaqfeh[2] is based on the migration of particles in the direction of the most unstable wavevector, which in the present case is the longest periodic direction perpendicular to gravity. Orientability of the particles in the disturbance flow is key to this mechanism, and a suspension of spherical particles is indeed known to be stable due to their isotropic mobility that prevents this lateral drift. At the particle level, suppression of the growth rate of fluctuations should therefore have a direct fingerprint on the horizontal migration of fibers, which in turn is intricately linked to the instantaneous orientation distribution of the filaments.

We first check that the migration of fibers is indeed towards regions of higher concentration. Figure 4 shows the ensemble-averaged mean velocity $\langle v_x \rangle$ and the number density distribution $p(N_x)$ in the horizontal (most unstable) direction at a specific time instant for the three representative cases. Both number density and velocity fields are averaged over the height and width of the simulation box so as to be a function of x only, and the velocity is normalized by the settling speed of an isolated vertical fiber. For cases A and B, when the flexibility-induced rotation is not overwhelmingly large, the drift of particles towards denser regions is evident, and so is the suppression of this mechanism by the strong horizontal reorientation due to flexibility in case C. The instantaneous orientation distribution determines, via Eq. (12), this drift velocity, and we look next to quantify this very microstructural link.

Figure 5 illustrates the key differences in lateral drift and orientation distributions between cases A–C, leading to the differences in the growth of number density fluctuations discussed above. We

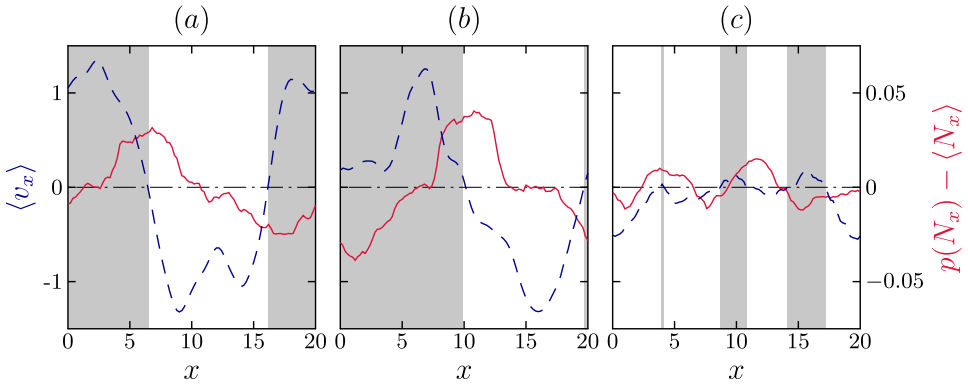

FIG. 4. Horizontal drift velocity $\langle v_x \rangle$ (blue dashed lines, axis on left) and number density distribution (red solid lines, axis on right) along the most unstable direction. The mean number density is subtracted from the distribution for clarity, and the shaded areas are meant to guide the eye towards regions where the measured drift is to the right (and to the left otherwise). (a), (b), and (c) represent one simulation corresponding to cases A, B, and C respectively, each at time $t = 1.00$.

define $\langle |v_x| \rangle$ as the ensemble-averaged mean of the absolute value of the velocity component in the x-direction perpendicular to gravity, which is the most unstable direction. We choose the absolute value as a quantifiable measure of the drift as opposed to the mean drift velocity $\langle v_x \rangle$ used above since the latter is zero due to symmetry and periodicity. This is plotted versus time in Fig. 5(a). We also show in Figs. 5(b)–5(e) the evolution of the orientation distribution $\psi(\theta)$ in each case, where θ denotes the polar angle between the fiber axis and the direction of gravity.

The effect of the base state is very clear at very short times $t \approx 0$, where the orientation distribution is nearly isotropic for case A but increasingly anisotropic and peaked around $\theta = \pi/2$ in cases B and C. The lateral drift velocity depends directly on the instantaneous orientation of a fiber. Due to the form of the settling velocity of an individual fiber following Eq. (5), particles migrate more slowly in the x-direction when oriented nearly perpendicular to gravity. This is evident from the values of $\langle |v_x| \rangle$ at $t \approx 0$, where cases B and C display much weaker drift than case A. In case B where the flexibility-induced reorientation is weak and the disturbance field immediately dominates the dynamics, the effect of the base-state anisotropy on suspension stability is seen in the rapid increase of $\langle |v_x| \rangle$ due to the rapid reorientation of the particles in a direction that facilitates migration. This is indeed the origin of the enhanced growth rate due to base-state anisotropy first proposed by Manikantan *et al.*[12] Particles in case *B* have a higher chance of being rotated by the disturbance field into

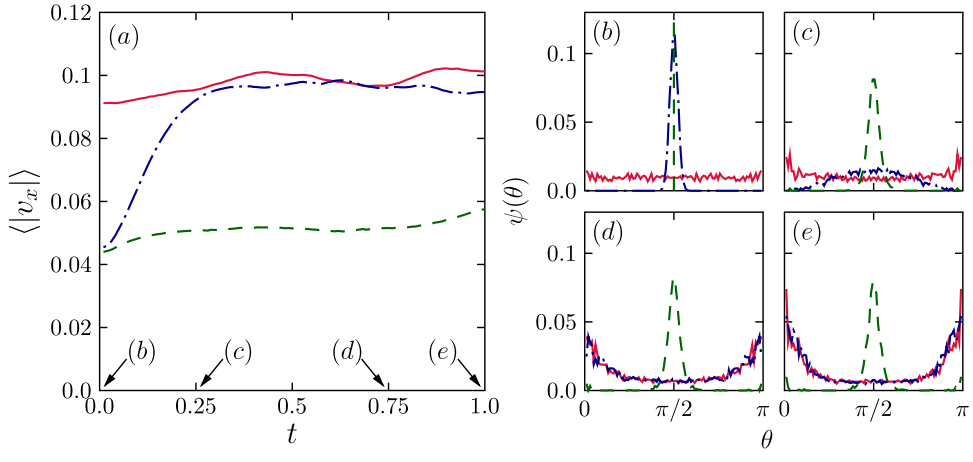

FIG. 5. (a) The effect of flexibility on mean horizontal drift velocities: case A is the red solid line, case B is the blue dashed-dotted line, and case C is the dotted green line. (b)–(e) show the corresponding orientation distributions averaged across all fibers in all simulations at times indicated by the arrows in (a).

configurations that allow them to migrate towards regions of larger concentration, thereby bolstering the instability.

In case C, however, we observe that flexibility-induced reorientation is sufficiently strong to maintain an anisotropic orientation distribution well past the initial growth of the instability. Correspondingly, the horizontal drift velocity remains much weaker than in cases A and B. This directly reflects the independent effect of flexibility. Particles now feel the competition between the disturbance velocity field that tends to orient them away from a nearly horizontal configuration and flexibility that tries to keep them horizontally aligned. For the value of β chosen in case C, the latter dominates at short times, which tends to slow the instability by hindering particle horizontal migration.

C. Stability of a well-stirred suspension

We have thus far used our simulations as a means to verify the predictions of the linear stability analysis of Manikantan *et al.*[12] Recall that the linear theory considers a Smoluchowski equation for the concentration field and perturbs it around a particular base state that solves the conservation equation exactly when the suspension is homogeneous in space. An arbitrary initial condition, however, is not amenable to a stability analysis the way it was performed because it may not solve a steady base state exactly. In the previous discussion, we initialized the particle configurations in our simulations according to the exact theoretical base state, assuming that such a state was somehow established prior to the onset of the instability. In a physical experiment, the initial stirring of the suspension is expected to lead to a random isotropic suspension, and the question remains whether the orientation distribution in that case would evolve towards the theoretical base state sufficiently fast for the predictions of the linear theory to hold, or whether the growth of the concentration instability would occur more rapidly. Here, we shed light on some of these questions using our simulations.

We have seen enough of the physics of the problem to postulate what might happen. If the suspension were to be isotropic in orientation at $t = 0$, we expect the effect of the base-state anisotropy to vanish. Flexibility-induced reorientation then only has one effect, namely, to oppose the rotation of the fibers towards orientations that cause them to be drawn into regions of higher concentration. This effect must become more significant as β decreases and always acts to suppress the instability. In other words, we expect a well-stirred suspension of weakly flexible fibers to experience, on average, a weaker concentration instability than in the benchmark case of a suspension of rigid rods.

Figure 6 summarizes the results of simulations corresponding to an initially isotropic particle distribution and confirms our hypothesis. Flexibility is seen to always suppress the instability, as demonstrated in Fig. 6(a) by the effective growth rate of the parameter d, which monotonically decreases with increasing flexibility (decreasing β). Figure 6(b) also shows the horizontal drift velocity, which should be contrasted with Fig. 5(a). In all cases, $\langle |v_x| \rangle$ now starts at the same value at $t = 0$,

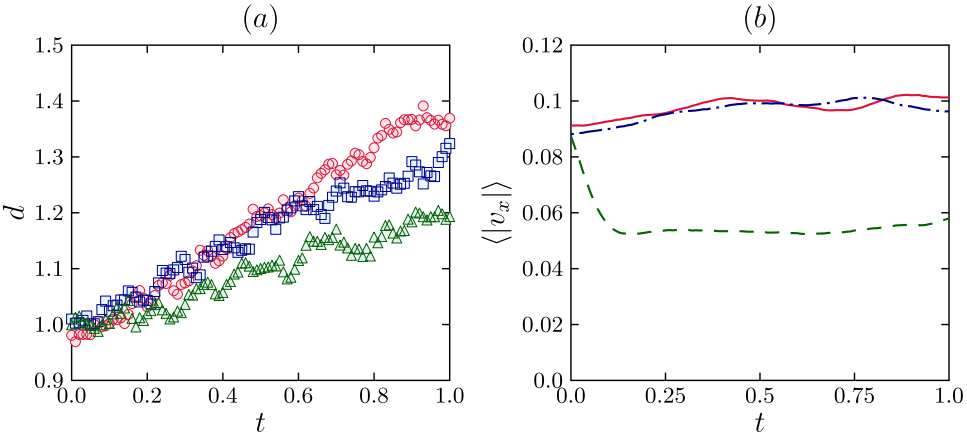

FIG. 6. The stability of a well stirred (initially isotropic) suspension. We now only see the independent effect of flexibility, as expected. Case A is in red (○ or a solid line), B is in blue (□ or a dashed-dotted line), and C is in green (△ or dashed line).

but is immediately suppressed in case C as a result of the rapid establishment of anisotropy in the orientation distribution leading to a weaker instability. In this case, the time scale over which the suspension evolves from the well-stirred isotropic distribution to the horizontally aligned configuration is fast compared to the growth of the instability. This time scale has a relevant effect only when β is sufficiently small, as we see no discernible difference for case B in the statistics of $\langle|v_x|\rangle$ — the leading-order effect of the base state predicted by the linear theory is absent here.

The stability analysis considered perturbations with respect to a steady base-state solution; a random isotropic suspension, however, solves no such base state. Nevertheless, our simulations reveal that the anisotropic orientation distribution corresponding to that steady state is quickly established in the case of sufficiently flexible fibers ($\beta = 0.01$). This is particularly evident in Fig. 6(b) where the absolute horizontal drift $\langle|v_x|\rangle$ rapidly evolves towards the values corresponding to the steady-state orientation distribution used in the stability analysis [compare with Fig. 5(a)], suggesting that the theoretical predictions still hold thereafter. Such is not the case of more rigid fibers ($\beta = 10$), for which the instability occurs before the base-state orientation distribution is achieved.

IV. CONCLUSION

In this paper, we have investigated the sedimentation of a suspension of weakly flexible fibers using particle simulations, in an attempt to shed light on the effect of fiber flexibility on the microstructural changes at the single particle level as well as on the stability of the suspension as a whole. We used the result from our previous work on individual elastic filaments to isolate the single additional effect of weak flexibility on the settling dynamics of a fiber, i.e., flexibility-induced reorientation. The effect of this reorientation on a suspension of such particles has already been studied using a linear stability on a mean-field model. The primary objective of the current study was to validate the predictions of the continuum model using simulations that captured the detailed dynamics of each fiber in the suspension.

We presented a numerical method for simulating large periodic systems of weakly flexible filaments, which we adapted from previous work on rigid particles. The entire set of evolution equations for the positions and orientations of N fibers was reduced to a set of matrix-vector multiplications only requiring knowledge of the current configuration of the particles in suspension. The calculation of these matrix-vector multiplications was further accelerated using the efficient SPME summation algorithm of Saintillan *et al.*[5] together with an approximate form for the determination of Brownian displacements based on diluteness, leading to a total computational cost of $O(N \log N)$.

We then went on to systematically study the effect of flexibility on suspension stability. Representative sets of parameters were chosen to most dramatically illustrate the different regimes of instability and the phenomena that demarcate them. Three cases were brought up repeatedly — one where the effect of flexibility was negligible, the second where flexibility-induced reorientation was known to establish an anisotropic base state leading to an enhancement of the growth of fluctuations, and the third where that same reorientation mechanism was strong enough to compete with rotation by the disturbance flow so as to impede the instability.

We first examined the evolution of number density fluctuations by means of a parameter $d(t)$ capturing the magnitude of fluctuations with respect the random Poisson distribution imposed at $t = 0$. The time evolution of d was shown to follow the trends predicted by the linear continuum theory. The effect of the anisotropic base state was seen to enhance the instability, while increasing flexibility further eventually impedes the growth of fluctuations. Extracting a short-time growth rate from the evolution of $d(t)$ allowed us to populate a phase diagram in β–Pe space, which showed excellent qualitative agreement with the theory.

A more detailed picture of the microstructural changes and their influence on stability was obtained by calculating the horizontal drift of the particles in the simulation. Recall that the mechanism of destabilization hinges on the ability of particles to migrate perpendicular to gravity towards regions of higher concentration. We saw that, on an average, the effect of the anisotropic base state alone is to enhance this horizontal migration as soon as the suspension is allowed to sediment. This verifies the hypothesized mechanism for an enhanced instability, i.e., a larger fraction of particles now reorient

in a way as to destabilize the suspension. The independent effect of flexibility, as expected, was seen to suppress this horizontal migration and prevent particle clustering by forcing particle orientations to remain close to horizontal.

Finally, we also used our simulations to analyze the case of a well-stirred suspension in which the initial orientation distribution is isotropic regardless of the values of β and Pe. This situation is outside the purview of the linear stability analysis performed on the mean-field model, but is perhaps the most relevant to describe experiments where the initial mixing of the suspension would lead to a random distribution. We speculated in this case that the destabilizing effect of the base state would vanish, and that flexibility would therefore only have a stabilizing effect. This was seen to be the case indeed — the number density fluctuations were shown to systematically decrease with increasing flexibility.

The effects of physically relevant considerations like walls and fluid inertia on flexible fiber suspensions are still open problems, theoretically as well as via simulations. While we expect the twofold consequences of flexibility to arise regardless, the relative strength of these effects may vary depending on the particular problem at hand. Future work might consider this problem from an experimental perspective, to which end we make it a point to note that our predictions are also valid for a suspension of weakly flexible fibers raising against gravity due to buoyancy, or more generally to any situation where a body force exists that causes particles to reorient perpendicular to it. Finally, we emphasize that we have primarily focused on short-time statistics in dilute systems with weak deformations; more detailed numerical methods would be needed to capture near-field lubrication interactions, entanglements, and particle shape deflections due to the disturbance field, all of which might become relevant over long times when local concentrations are sufficiently large.

ACKNOWLEDGMENTS

We thank Saverio Spagnolie and Lei Li for useful conversations on this work and gratefully acknowledge support from NSF Grant No. CBET-1150590.

[1] É. Guazzelli and J. Hinch, "Fluctuations and instability in sedimentation," Annu. Rev. Fluid Mech. **43**, 97–116 (2011).
[2] D. L. Koch and E. S. G. Shaqfeh, "The instability of a dispersion of sedimenting spheroids," J. Fluid Mech. **209**, 521–542 (1989).
[3] B. Herzhaft, É. Guazzelli, M. B. Mackaplow, and E. S. G. Shaqfeh, "Experimental investigation of the sedimentation of a dilute fiber suspension," Phys. Rev. Lett. **77**, 290 (1996).
[4] B. Metzger, J. E. Butler, and É. Guazzelli, "Experimental investigation of the instability of a sedimenting suspension of fibres," J. Fluid Mech. **575**, 307–332 (2007).
[5] D. Saintillan, E. Darve, and E. S. G. Shaqfeh, "A smooth particle-mesh Ewald algorithm for Stokes suspension simulations: The sedimentation of fibers," Phys. Fluids **17**, 033301 (2005).
[6] K. Gustavsson and A.-K. Tornberg, "Gravity induced sedimentation of slender fibers," Phys. Fluids **21**, 123301 (2009).
[7] D. Saintillan, E. S. G. Shaqfeh, and E. Darve, "The growth of concentration fluctuations in dilute dispersions of orientable and deformable particles under sedimentation," J. Fluid Mech. **553**, 347–388 (2006).
[8] B. D. Hoffman and E. S. G. Shaqfeh, "The effect of Brownian motion on the stability of sedimenting suspensions of polarizable rods in an electric field," J. Fluid Mech. **624**, 361–388 (2009).
[9] A. Dahlkild, "Finite wavelength selection for the linear instability of a suspension of settling spheroids," J. Fluid Mech. **689**, 183–202 (2011).
[10] X. Xu and A. Nadim, "Deformation and orientation of an elastic slender body sedimenting in a viscous liquid," Phys. Fluids **6**, 2889 (1994).
[11] L. Li, H. Manikantan, D. Saintillan, and S. E. Spagnolie, "The sedimentation of flexible filaments," J. Fluid Mech. **735**, 705–736 (2013).
[12] H. Manikantan, L. Li, S. E. Spagnolie, and D. Saintillan, "The instability of a sedimenting suspension of weakly flexible fibres," J. Fluid Mech. **756**, 935–964 (2014).
[13] J. E. Butler and E. S. G. Shaqfeh, "Dynamic simulations of the inhomogeneous sedimentation of rigid fibres," J. Fluid Mech. **468**, 205–237 (2002).
[14] H. Hasimoto, "On the periodic fundamental solutions to the Stokes equations and their application to viscous flow past a cubic array of spheres," J. Fluid Mech. **5**, 317–328 (1959).
[15] A.-K. Tornberg and M. J. Shelley, "Simulating the dynamics and interactions of flexible fibers in Stokes flows," J. Comput. Phys. **196**, 8–40 (2004).
[16] H. Manikantan and D. Saintillan, "Subdiffusive transport of fluctuating elastic filaments in cellular flows," Phys. Fluids **25**, 073603 (2013).
[17] G. K. Batchelor, "Slender-body theory for particles of arbitrary cross-section in Stokes flow," J. Fluid Mech. **44**, 419–440 (1970).

[18] O. G. Harlen, R. R. Sundararajakumar, and D. L. Koch, "Numerical simulations of a sphere settling through a suspension of neutrally buoyant fibres," J. Fluid Mech. **388**, 355–388 (1999).
[19] Y. Saad and M. H. Schultz, "GMRES: A generalized minimal residual algorithm for solving nonsymmetric linear systems," SIAM J. Sci. Stat. Comput. **7**, 856–869 (1986).
[20] M. Fixman, "Construction of Langevin forces in the simulation of hydrodynamic interaction," Macromolecules **19**, 1204–1207 (1986).
[21] A. J. Banchio and J. F. Brady, "Accelerated Stokesian dynamics: Brownian motion," J. Chem. Phys. **118**, 10323–10332 (2003).
[22] D. Saintillan, E. Darve, and E. S. G. Shaqfeh, "Hydrodynamic interactions in the induced-charge electrophoresis of colloidal rod dispersions," J. Fluid Mech. **563**, 223–259 (2006).
[23] M. Fixman, "Simulation of polymer dynamics. I. General theory," J. Chem. Phys. **69**, 1527–1537 (1978).
[24] P. S. Grassia, E. J. Hinch, and L. C. Nitsche, "Computer simulations of Brownian motion of complex systems," J. Fluid Mech. **282**, 373–403 (1995).